Electron Dynamics in Dye-Sensitized Solar Cells: Effects of Surface Terminations and Defects

Zi Li, Xu Zhang, and Gang Lu*

Department of Physics and Astronomy, California State University Northridge, California 91330-8268, United States

Received: September 8, 2010; Revised Manuscript Received: October 22, 2010

The electron dynamics in a TiO_2/alizarin based dye-sensitized solar cell is studied by a means of ab initio nonadiabatic molecular dynamics. The effects of surface terminations and vacancy defects on photoexcited interfacial electron transfer (ET) and energy relaxation of injected electrons are examined in detail. In particular, we consider three plausible TiO_2 surface terminations which are stable at zero temperature. However, only one of them maintains structural integrity at room temperature while the other two terminations lead to broken interfacial Ti−O bonds. An ultrafast ET dynamics (4.6 fs) is observed for the intact interface, consistent with relevant experimental and theoretical results. On the other hand, the ET dynamics of the two other terminations takes either a much longer time or results in less charge transfer. The surface vacancies in TiO_2 are found to play important roles in the structural integrity, the interfacial ET dynamics, and the energy relaxation in the TiO_2 conduction bands. For example, O vacancies are observed to enhance the interfacial bonding, delocalize the photoexcited state, and facilitate nonadiabatic ET. On the other hand, Ti vacancies give rise to less stable interfacial structure and negligible ET. The energy relaxation time scale for the injected electron in the conduction band is 500 fs regardless of the vacancies. Both O and Ti surface vacancies are found to trap the injected electron while the O vacancies could increase the charge recombination at the interface.

Introduction

Dye-sensitized solar cells (DSSCs) or Grätzel cells are among the most promising alternatives to the silicon-based traditional solar cells.[1] The Grätzel cells are made of low-cost and environmentally friendly materials and do not need elaborate apparatus to be manufactured into flexible sheets with mechanical robustness. The energy efficiency of a single DSSC has reached 11%, comparing to less than 6% of efficiency for polymer based solar cells.[2] Further development of the DSSCs demands a better understanding of the limiting factors that influence the performance of the cells. In a DSSC, nanocrystalline semiconductor oxides, mostly TiO_2, are used as the electrode and merged into an electrolyte solution containing dye molecules and redox mediators. Therefore water molecules are often present in the solution,[3−6] leading to the saturation of dangling bonds at the semiconductor surface. The semiconductor surface terminations may involve both molecular and dissociative adsorptions of the water,[7−10] and in the latter case the orientations of the OH groups and the H atoms may change randomly in the solution. As a result, the interfacial bonding between the semiconductor and the dye molecule could be affected significantly by the surface termination which gives rise to drastically different electron-transfer (ET) dynamics. On the other hand, due to the large surface-to-volume ratios of the nanocrystalline semiconductor films, surface defects such as vacancies are expected to influence the performance of the solar cells.[3−5,11−15] These surface defects can introduce defect levels, modify the molecular and electronic structures at the interface, and trap the charge carriers, resulting in different electron-transfer and relaxation dynamics, as well as the charge recombination rates.

* To whom correspondence should be addressed: E-mail: ganglu@csun.edu.

At the semiconductor/dye interface, the photoexcited (PE) electrons are transferred from the dye molecule's lowest unoccupied molecular orbital (LUMO) to the semiconductor's conduction band (CB) to contribute the photocurrent of the DSSC. This interfacial ET dynamics is of crucial importance to the efficiency of the DSSC and has been the subject of many experimental[3−6,16−21] and theoretical investigations.[17,22−37] The electron transfer in the DSSC is ultrafast with a time scale less than 100 fs;[3,16−18] in particular, a 6 fs ET has been observed recently.[18] On the theoretical side, various simulation methods, from empirical models[17,22,23,38−40] to the time-dependent density functional theory (TDDFT)[24,26−28,41,42] have been employed to simulate the ET process in DSSCs. For example, Meng and Kaxiras have used TDDFT to examine ET at the interface between a TiO_2 nanowire and organic dye molecules. They have systematically studied important factors that influence ET dynamics and obtained general trends which could be useful for future development of DSSCs. De Angelis et al. have used TDDFT to examine the effect of the dye protonation on the electronic properties of N719-sensitized TiO_2 particles as well as the effects of the dye adsorption mode on the open-circuit voltage.[41,42] Using an ab initio nonadiabatic molecular dynamics (NAMD) method, Prezhdo and collaborators have considered various electron dynamics in DSSCs, including electron injection from dye to TiO_2 CB, electron relaxation within TiO_2 CB, and back-electron-transfer processes, etc. Their work has shed light on the fundamental electronic processes that contribute to the overall efficiency of DSSCs, notwithstanding their work has focused only on the perfect systems.

In this paper, we study the photoexcited electron dynamics across the interface between rutile TiO_2 (001) surface and an alizarin dye molecule as well as the energy relaxation dynamics of the injected electron in the TiO_2 CB using the NAMD method.[26] The goal is to elucidate the effects of TiO_2 surface

10.1021/jp108590f
Published on Web 12/06/2010

terminations and surface defects on the ET and energy relaxation dynamics. To this end, three different surface terminations and four different surface vacancy defects are examined in detail.

Computational Method and Models

Ab Initio Nonadiabatic Molecular Dynamics. The interfacial ET dynamics is determined by the ab initio NAMD originally proposed by Prezhdo et al.[26,29−37] In this method, the coupled electron-ion dynamics could be described by both Ehrenfest[43] and surface hopping formalisms.[44,45] The PE state is expressed in the basis of adiabatic Kohn−Sham (KS) orbitals that are obtained by the time-independent DFT calculation for the current ionic configuration **R** at each MD step and is evolved in real time.

The ET at a given time can be characterized by the amount (or the fraction) of the PE electron remaining at the dye molecule,

$$\mathrm{ET}(t) = 1 - \sum_{i,j} c_i^* c_j \int_{\mathrm{dye}} \phi_i^*(\mathbf{r}, \mathbf{R}(t))\, \phi_j(\mathbf{r}, \mathbf{R}(t))\, \mathrm{d}\mathbf{r} \tag{1}$$

where i and j are summed over all relevant KS orbitals, c_i and c_j are expansion coefficients of PE state, ϕ_i and ϕ_j are the adiabatic KS orbitals, and the integration is over the volume of the dye molecule. Taking the time derivative of eq 1, we obtain two contributions

$$\frac{\mathrm{d}}{\mathrm{d}t}\mathrm{ET}(t) = -\sum_{i,j}\left\{\frac{\mathrm{d}c_i^* c_j}{\mathrm{d}t}\int_{\mathrm{dye}} \phi_i^*(\mathbf{r}, \mathbf{R}(t))\, \phi_j(\mathbf{r}, \mathbf{R}(t))\, \mathrm{d}\mathbf{r} + c_i^* c_j \frac{\mathrm{d}\int_{\mathrm{dye}} \phi_i^*(\mathbf{r}, \mathbf{R}(t))\, \phi_j(\mathbf{r}, \mathbf{R}(t))\, \mathrm{d}\mathbf{r}}{\mathrm{d}t}\right\} \tag{2}$$

The first term represents the nonadiabatic electron transfer, corresponding to the changes in the occupation of the adiabatic states; that is to say that the PE electron hops from one state to another to accomplish ET. The second term represents the adiabatic contribution, corresponding to the changes in the adiabatic states themselves. In this case, the PE electron remains in the same KS orbitals while these orbitals evolve in space, leading to ET. The sum of nonadiabatic (NA) ET, adiabatic ET, as well as the initial ET at $t = 0$ gives rise to the total ET.

To describe the energy relaxation of the injected electron in the TiO_2 conduction band, a simplified version of the FSSH method[44,45] is used. In FSSH, the PE electron always stays at one adiabatic KS state at any time, but it can hop from one adiabatic KS state to another. The hopping probability is related to the expansion coefficients $c_j(t)$ that are evolving in the same way as in the Ehrenfest dynamics. FSSH satisfies the detailed balance,[46,47] which is important for studying the energy relaxation process. In the simplified FSSH[34] method, a hop rejection in the traditional FSSH is replaced by multiplying the hop probability with the Boltzmann factor for an energetic upward transition; this simplification can significantly reduce the computational effort and at the same time give a reasonable description of the electron relaxation.

Computational Models and Parameters. Although TiO_2 nanoparticles in anatase phase are often used in the state-of-the-art DSSCs, we choose to work on the rutile phase in this paper because it is energetically more stable than the anatase phase for bulk structures.[7] On the other hand, although the (110) rutile surface is more stable than the (001) surface, the surface reaction between water and the (110) surface is more complex and controversial;[8,9] therefore we decide to focus on the (001) surface instead. In addition, the ET dynamics at the perfect rutile (001) surface/alizarin system has been examined before, to which we can compare the results. The rutile TiO_2 (001) surface is modeled with a five-atomic-layer slab partially shown in Figure 1. The dangling bonds at both top and bottom surfaces of the TiO_2 slab are saturated by two OH groups on each terminal titanium (Ti) atom and by one hydrogen (H) atom on each terminal oxygen (O) atom, as suggested by experiments.[9] The bottom two layers of the slab including the saturating atoms are fixed in the MD simulations. The alizarin molecular bonds to a terminal Ti atom through two O atoms (O1 and O2), as indicated in Figure 1a. This structure is found to be the most stable by DFT calculations[48] and has been used in the simulations of ET dynamics.[32−35] In the direction perpendicular to the surface, large vacuum layers are used, leading to a lattice constant of 30 Å in the normal direction. The periodical boundary conditions are also used in the other two directions, with a lattice constant of 9.26 Å.

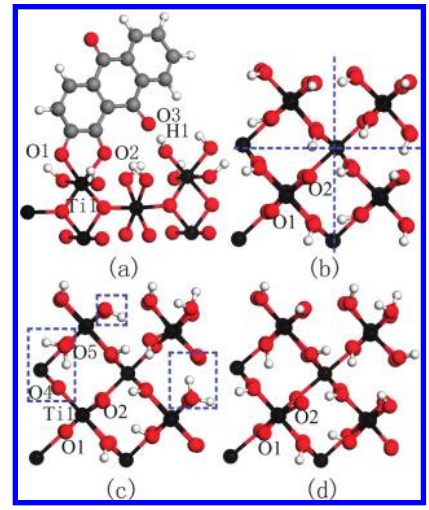

Figure 1. Optimized structures of TiO_2/alizarin systems. The red, gray, white, and black spheres represent O, C, H, and Ti atoms, respectively; some of the key atoms are labeled. (a) The interfacial structure (side view) is shown with the alizarin attached to the TiO_2 surface via the interfacial Ti1−O1 and Ti1−O2 bonds. Panels b−d display the top view of the three different surface terminations of I−III, respectively; only the O atoms of the alizarin bonding to Ti are shown and labeled by O1 and O2. Some TiO_2 layers farther away from the surface are omitted for clarity. In b, the orientations of the H atoms are similar in the four parts divided by the dashed lines. In d, the H positions in the upper two parts are opposite to those in b. In c, some variations of the H positions are introduced from those in d, as indicated in the dashed boxes.

The ab initio molecular dynamics is performed by using VASP code[49,50] based on DFT with the plane-wave basis and ultrasoft pseudopotentials. The PW91 functional[51] is used for the generalized gradient correction. The softer pesudopotentials for O and C atoms are used since they can make the alizarin LUMO slightly lower than the TiO_2 CB edge (CBE), which has been found by the combined experimental[3] and theoretical[52] analysis of the adsorption spectra. These softer pesudopotentials lead to 210 eV energy cutoff.

The system structure is initially optimized to an energy minimum by static relaxations; then the system is heated to 300 K with a 100 fs MD run, and stays at 300 K for 1000 fs to reach the thermal equilibrium. Finally, another 1000 fs micro-canonical MD production run is performed to compute the

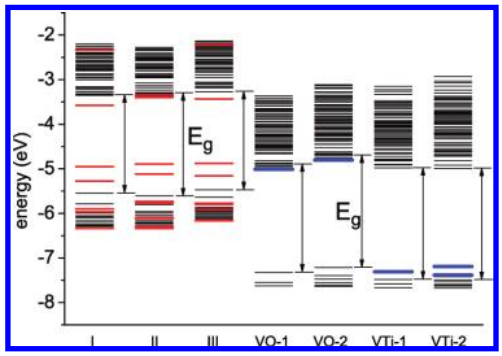

Figure 2. Energy diagrams of the three perfect structures I−III and of VO-1, VO-2, VTi-1, and VTi-2 (see text for their definitions). The red lines in structures I−III indicate the energy levels primarily contributed from the alizarin. The blue lines represent the defect levels.

necessary electronic structure information for which the electron dynamics can be determined. In the electron dynamics simulations, 100 MD trajectories each 100 fs long are used to calculate the ensemble average; the averaging turns out to be crucial for capturing the stochastic nature of the coupled dynamics. These 100 trajectories are chosen from the production MD run with 100 different starting points. For each trajectory, the TDDFT equation is integrated with a time step of 10^{-3} fs.[33] Because the time scale for the injected electron relaxation in the TiO_2 CB is considerably longer than that in interfacial ET, a 5000 fs microcanonical MD production run is performed to produce 300 TDDFT trajectories, each 2000 fs long. For the interfacial ET dynamics, the initial PE state is chosen from the low-lying empty states with the largest localization at the molecule. On the other hand, for the electron relaxation in the TiO_2 CB, the initial electronic state is selected from a CB state with a large density of states (DOS).

Results and Discussion

Effects of Surface Terminations. To study the effects of surface terminations, three different terminal H and OH orientations are considered as examples in Figure 1b−d with their differences explained in the caption. The three terminations labeled by I, II, and III have similar band structures, as shown in Figure 2. The alizarin's highest occupied molecular orbital (HOMO) is located well inside the TiO_2 band gap (E_g), and the alizarin LUMO is a slightly lower than the CBE; both are consistent with the combined experimental and theoretical analysis.[4,52] Therefore, although E_g is underestimated, the relative energy level alignment between the alizarin LUMO and TiO_2 CB is well-captured by the DFT simulations.

Although the equilibrium structures of the three terminations are rather similar, their ionic dynamics at 300 K turns out to be markedly different. From the MD simulations, we find that, in structures I and II, one of the two Ti−O bonds between the TiO_2 and the alizarin is broken, while, in structure III, both Ti−O bonds remain intact. The distinctive ionic dynamics can be understood from the minor differences in the equilibrium structures as summarized in Table 1. For example, as shown in Figure 1a, O3 atom in structure I is rather close to H1 atom (1.41 Å), leading to a strong interaction between the two atoms. This interaction in turn weakens the Ti1−O2 bond—the bond length of 2.15 Å is longer than those in structures II and III—resulting in a broken Ti1−O2 bond during the MD simulations. On the other hand, the O4 atom in structure II loses its H to the nearby O5 and thus bonds more strongly with Ti1 atom. Therefore the Ti1−O1 and Ti1−O2 bonds between the TiO_2 and the alizarin are weakened and eventually broken in the MD simulations. These structural differences could lead to drastically different interfacial ET dynamics, as described in the following.

TABLE 1: Bond Lengths (Å) of Ti1−O1, Ti1−O2, and O3−H1 in Structures I−III, As Labeled in Figure 1

	I	II	III
Ti1−O1	1.97	2.02	2.01
Ti1−O2	2.15	2.04	2.09
O3−H1	1.41	1.53	1.59

Panels a, c, and e of Figure 3 display the time evolution of the energy levels of the PE state and CBE states in the 1000 fs microcanonical MD run. Due to the thermal motion of the ions, the energy levels fluctuate considerably, especially for the PE state. In comparison with III, the larger energy fluctuations in I and II are probably due to their less stable structures; the energy oscillation of CBE is relatively small for the rigid structure of TiO_2. For structure I, the PE state energy level is well-separated from those of TiO_2 CBE states, leading to an inefficient and negligible ET across the interface. For structure II, the energy overlap between the PE state and CBE states occurs about half of the time, resulting in an appreciable ET. In structure III, the energy overlap is much better than those in both I and II, and thus the ET is the most efficient.

The corresponding ET dynamics can be characterized by the amount of ET—the fraction of the PE electron that has left

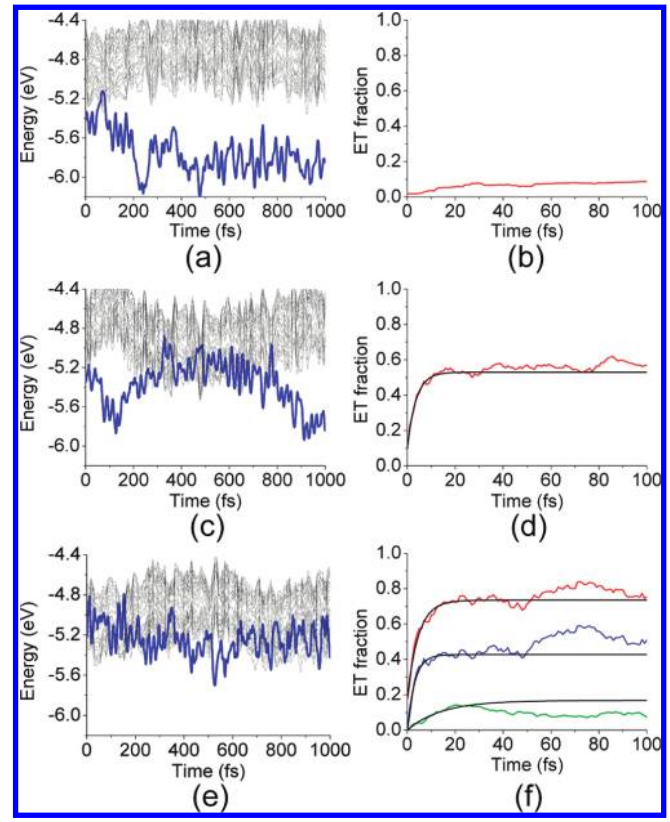

Figure 3. Time evolution of the PE state energy (blue) and the CBE states energies (black) for structure I (a), structure II (c), and structure III (e). The corresponding electron-transfer curves are displayed in b, d, and f. The red curves represent the computed total fraction of charge transfer, and the black curves are the fits to eq 3. In f, the three curves from top to bottom correspond to the total (red), adiabatic (blue), and nonadiabatic (green) part of ET.

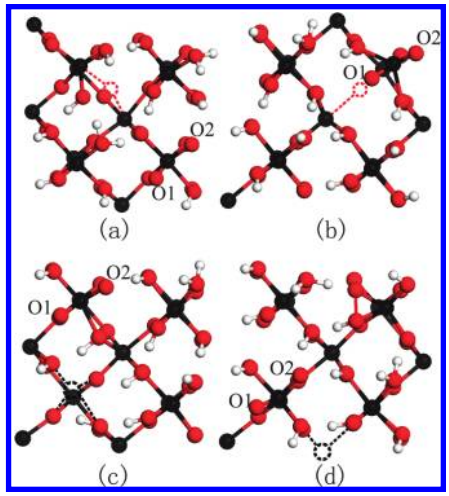

Figure 4. Structures of the surface vacancies (top view) for (a) VO-1, (b) VO-2, (c) VTi-1, and (d) VTi-2. The O and Ti vacancies are labeled by red and black circles, respectively. Only the O atoms of the alizarin bonding to Ti are shown and labeled.

the molecule—as a function of time, shown in Figure 3b,d,f. The fractions are fitted to the following equation[33]

$$\mathrm{ET}(t) = \mathrm{ET}_f(1 - \exp[-(t + t_0)/\tau]) \qquad (3)$$

where ET_f is the final amount of ET and τ is the estimated elapsed time for ET, a key quantity that represents the efficiency of interfacial ET. Since there is always a small fraction of the PE state residing at TiO_2 at $t = 0$, t_0 (the intercept of the t-axis) can be interpreted as the ET time corresponding to the pretransferred amount.

For structure I, the total amount of the charge transfer within the 100 fs TDDFT simulation time is less than 10% with the corresponding ET time scale being much longer than 100 fs, which implies a poor performance of the solar cell. For structure II, the total amount of the charge transfer within 100 fs is only about 50% and the corresponding ET time scale is 3.6 fs. For structure III, the total amount of charge transfer within 100 fs is about 70% and the corresponding time scale of ET is 4.6 fs, which is close to the previous theoretical result of 7.9 fs[33] and agrees very well with the experimental value of 6 fs.[18] The ET time scale for structure II is similar to that for structure III because the ET time is much faster than the time span (~500 fs) that the PE energy level overlaps with the CBE for structure II; therefore the ET can be completed within this time span. The fact that the total ET is about 0.5 suggests that the ET does not take place within the 100 fs time interval for half of the trajectories. Furthermore, since the final amount of charge transfer in structure II is smaller than that in structure III, the corresponding short-circuit current would be smaller as well, leading to a lower efficiency.

Effects of Vacancy Defects on ET. We next consider the effects of vacancy defects on the ET process. To this end, two O vacancy configurations and two Ti vacancy configurations have been studied, although the focus of this section is on the O vacancies. The atomic structures of the O vacancy in the first layer (VO-1) and in the second layer (VO-2) and Ti vacancy in the first layer (VTi-1) and in the second layer (VTi-2) are shown in Figure 4a–d, respectively. For VO-1 and VTi-1, one H atom and two OH groups connected to the vacancy atom are also removed, respectively. Although Ti vacancies are not observed under normal experimental conditions, they exist nonetheless; thus, we include them here for completeness. Although only termination I is considered here, the O vacancy defect structures of all three terminations are actually thermodynamically stable in the MD simulations; this is in contrast to the prefect cases in which only structure III is stable.

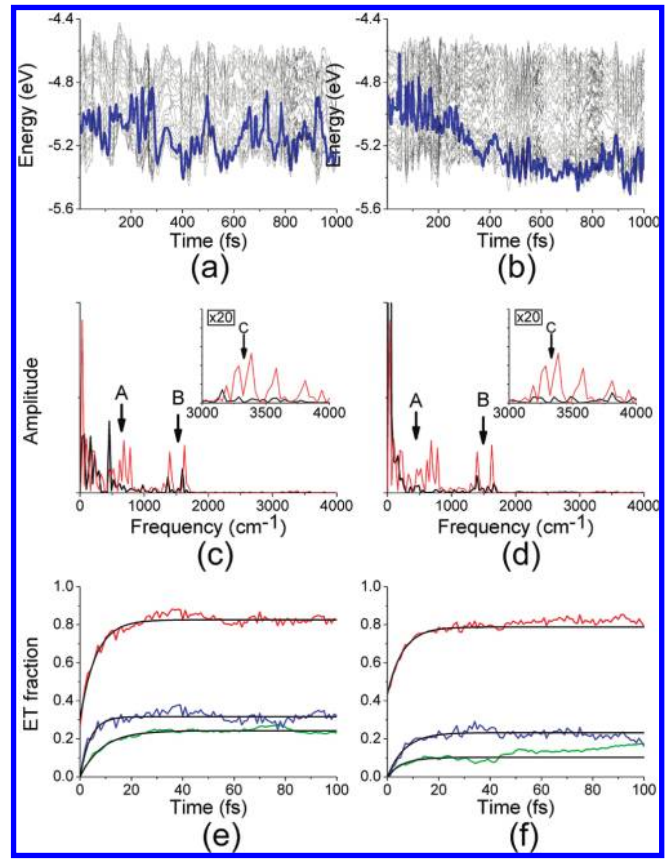

Figure 5. Electron dynamics for VO-1 (left column) and VO-2 (right column). Panels a and b display the time evolution of the PE state energy (blue) and CBE states energies (black). Panels c and d show the Fourier transform (FT) of the PE state energy (black); the red curves correspond to the FT of the PE state energy in the perfect structure III. The insets are the blown-up view (×20) at higher frequencies around 3500 cm^{-1}. Panels e and f represent the electron-transfer fraction; the three curves correspond to the total ET (red), adiabatic ET (blue), and nonadiabatic ET (green) part. The black curves are the exponential fits.

Parts a and b of Figure 5 display the time evolution of the energy levels for the defect systems. For both VO-1 and VO-2, the PE state energy level overlaps very well with the CB. Additionally, in comparison with the prefect structure III where the PE state energy moves in and out of the CB (the PE level fluctuates both above and below the CBE), the PE state level in VO-1 and VO-2 fluctuates only above the CBE. Therefore it is expected that the ET is more efficient in the presence of the O vacancies. More importantly, in the presence of the O vacancies, the energy difference between the HOMO and TiO_2 CBE decreases from 1.61 to 1.42 eV and to 1.38 eV for VO-1 and VO-2, respectively, which could lead to a lower open-circuit voltage; this is because the voltage is determined by the potential difference between CBE and the redox level of electrolyte, and the redox level is higher than the HOMO.

The Fourier transforms (FT) of the PE energy of VO-1 and VO-2 are shown (black curves) in Figure 5c,d, and the corresponding FT for the perfect structure III is also shown for comparison (red curves). For the perfect system, the peaks below 700 cm^{-1} (A) correspond to bending and torsional motions of the dye molecule; the peaks around 1600 cm^{-1} (B) arise from

TABLE 2: Fitted ET Time Scale for the Perfect Structure III, and VO-1 and VO-2 Systems[a]

	III	VO-1	VO-2
total	4.6	6.1	6.0
adiabatic	3.1	4.0	6.7
NA	14.2	8.6	5.7

[a] The adiabatic ET and nonadiabatic (NA) ET time scales are also listed. The unit is femtoseconds.

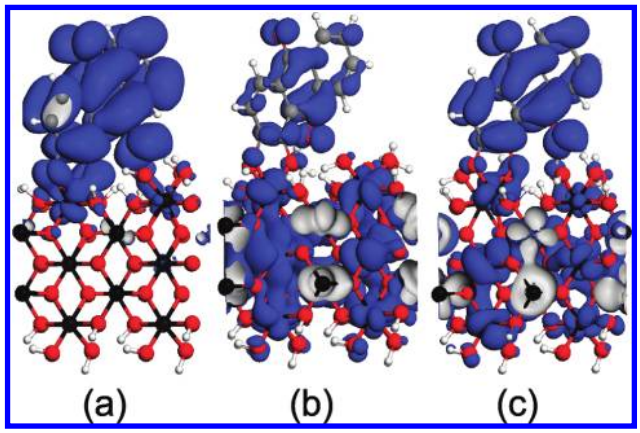

Figure 6. PE state charge density for (a) the perfect structure III, (b) VO-1, and (c) VO-2. The value of the isosurface is 0.001 e/Å^3.

C—C and C═O stretches; the small peaks near 3300 cm^{-1} (C) are associated with O—H stretches. The presence of the C peaks suggests that the terminal OH groups could influence the PE energy, thus the charge transfer in the prefect system. In comparison with the perfect structure, the corresponding peak positions for the defect systems shift to lower frequencies, especially for the A peaks. The fact that the C peaks nearly vanish in the defect systems indicates that the effect of the terminal H is negligible in the presence of the O vacancies.

The ET dynamics for VO-1 and VO-2 is shown in Figure 5e,f, respectively. The ET contributions are classified into the adiabatic and the nonadiabatic processes as defined in eq 2. Comparing to the perfect structure III, the NA ET in the defect systems is faster (see Table 2) because (i) the PE state energy is inside the CB of TiO_2, which facilitates the charge hopping across the interface, and (ii) the NA injection rate is proportional to the acceptor DOS.[36] On the other hand, the adiabatic ET in the defect systems is slower than the perfect structure, which can be attributed to the slower motions of the dye molecule, evidenced by the red shift in the phonon spectrum in Figure 5. Since there is a strong Ti—O bonding between alizarin and TiO_2, the adiabatic ET is dominant;[36] hence, the overall ET time scale is still slightly longer for the defect systems. We have also determined the initial and final amounts of ET in the defective and perfect systems; the initial and final fractions of the PE electron are 0.31 and 0.83 for VO-1, 0.46 and 0.79 for VO-2, and 0.18 and 0.73 for the perfect structure III. In comparison with the perfect system, both the initial and the final fractions of the ET are greater in the defect systems, suggesting that the O vacancies could assist ET, partially due to the vacancy-induced delocalization of the PE state onto TiO_2. This delocalization can be seen from the PE charge density plot at the equilibrium structures in Figure 6. For both VO-1 and VO-2, the PE state charge density is more delocalized, spreading over to both the molecule and TiO_2, which is significantly different from the charge distribution in the perfect structure III. Meng and Kaxiras[15] have also observed that the O vacancies could enhance ET from dyes to TiO_2, although their dye molecules and TiO_2 surface are different from ours. Therefore, the mechanism in which the O surface vacancies facilitate the interfacial ET appears to be general in DSSCs.

We have also considered Ti vacancy at different surface layers for both structures I and III. However, we find that these defect structures are not stable in the sense that one (or two) Ti—O bond between the molecule and TiO_2 is broken during the MD simulations. As a result, the ET processes in these structures are rather inefficient, but the detailed results are not shown here.

Effects of Vacancy Defects on Energy Relaxation. The surface defects also influence the energy relaxation once the PE electron is injected into the TiO_2 CB. It is well-known that point defects in a semiconductor can introduce defect states in the band gap, as we have observed for both the O and Ti vacancies. For the oxygen vacancy systems, there is one *occupied* energy level slightly below the TiO_2 CB (Figure 2) which corresponds to the donor state in an n-type semiconductor. The shallow donor state introduced by the O vacancies has also been predicted by others.[53,54] Although this donor state is occupied at the ground state, the electron at this state can be thermally excited to vacate the state so that the energy relaxation to the donor state can take place. For the VTi-1 system where a Ti atom is removed—along with two OH groups at the first layer—an *empty* defect level appears slightly above the TiO_2 valence band (VB), representing an acceptor state. When a Ti vacancy is introduced at the second layer of the surface (VTi-2), there form two acceptor states above the VB. These donor and acceptor states extend to the entire simulated system, consistent with experimental observations.[55]

As the PE electron is injected into the TiO_2 CB, we assume it takes a CB state with a high DOS, as indicated by the arrow in Figure 7a.[34] Since its energy is 1.6 eV higher than the CBE, it shall relax in energy within the TiO_2 CB and eventually reach the CBE. Therefore this energy relaxation process can be studied by projecting the injected electron state onto three lowest CB states and examine how the population on these states evolves as a function of time. As shown in Figure 7, for the perfect structure I, the stabilized population of the CBE state is about 50% and the CBE+1 state about 30%. The population of the CBE+2 state increases to 20% and then decreases, showing a transient feature due to its higher energy. The time scale for the injected electron relaxation to the CBE is about 500 fs, 2 orders of magnitude larger than the time scale for the interfacial electron transfer.

For VO-1 and VO-2 systems, the donor state can accommodate half of the injected electron at 2000 fs; the populations of the CBE and CBE+1 states are smaller than that of the perfect system, suggesting that the injected electron is bound to (or trapped by) the defect. For VTi-1, the acceptor state is slightly above the VB and much lower than the CB and the injected state. Therefore it takes a longer time for the electron to relax to the defect state. The population of the defect state increases linearly to 50% at 2000 fs; thus, the relaxation time is about 4000 fs assuming the linear relation persists. The population of the CB states reaches the maximum at 600—1000 fs and then decays continuously. Therefore, the surface Ti vacancy appears to be a strong trapping center for the injected electron. For the VTi-2 system, since there are two defect states, the electron relaxation process is faster than that for the VTi-1 system; the population of the defect states reaches 70% at 2000 fs. One of the defect states which is higher in energy becomes saturated at 800 fs, while the other (lower energy) continuously traps an electron. Finally, we find that the perfect and defect systems have the similar relaxation time of ~500 fs, although the

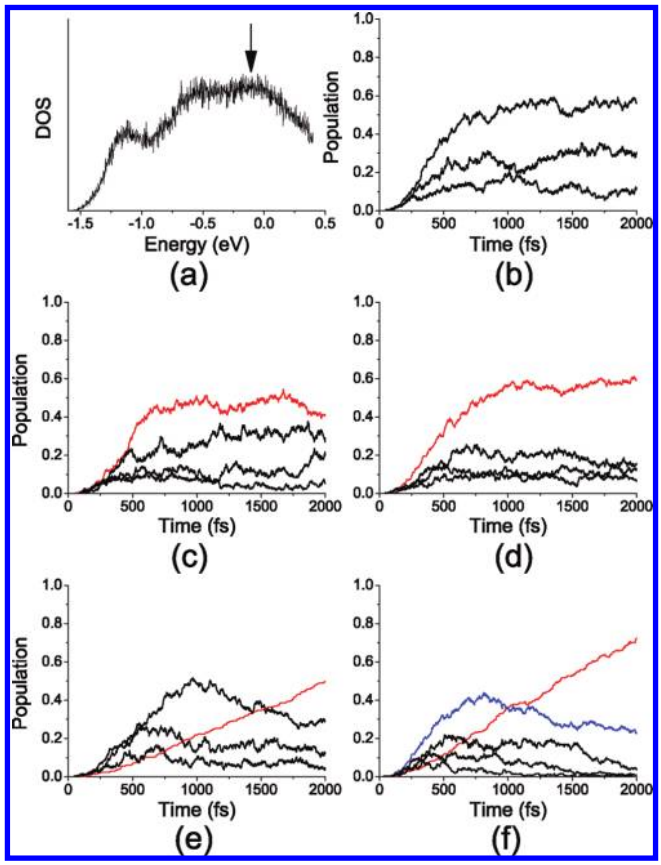

Figure 7. Energy relaxation in the CB. (a) The density of states of the perfect structure I is averaged over 5000 MD time steps; the arrow indicates the energy of the injected electron. Panel b shows the population evolution of the CBE states of the perfect system. Panels c−f display the population evolution of VO-1, VO-2, VTi-1, and VTi-2 systems, respectively; the red (blue) and black curves represent the defect levels and the CBE states, respectively. In f, the red and blue curves correspond to the lower and higher defect levels, respectively.

population distribution is rather different. Being trapped by the surface defects, the injected electron is prevented from diffusing into the bulk and becomes spatially very close to the dye. Because the O defect energy level is higher than the HOMO of the dye, the charge recombination (between the injected electron at the TiO_2 surface and the hole at the dye) may increase in the presence of the O vacancies. On the other hand, since the Ti defect energy levels are lower than the HOMO, the recombination is less likely to occur.

Conclusions

Ab initio NAMD simulations are performed to study the electron dynamics in the TiO_2/alizarin system, focusing on the effects of the surface terminations and the vacancy defects. We have considered three plausible surface terminations for which the structure stability and the interfacial ET dynamics are examined. Although the three structures are stable at zero temperature, only one of them remains stable in the MD simulations without breaking the interfacial Ti−O bonds. For this surface termination, an ultrafast (∼4.6 fs) ET is observed, which is consistent with the experimental and theoretical results. As expected, the ET process in the other two surface terminations takes either much longer time or results in less charge transfer, leading to a smaller short-circuit current. The O vacancies are observed to enhance the bonding across the interface; they also introduce the donor states and lift the LUMO into the CB of TiO_2, which results into a better energy alignment and a faster nonadiabatic ET. In addition, they delocalize the PE state and promote more charge transfer. However, the O vacancies also raise the alizarin HOMO energy and result in a smaller open-circuit voltage. On the other hand, the Ti vacancies give rise to the less stable structures and the negligible interfacial ET. The energy relaxation time scale for the injected electron is about 500 fs regardless of the vacancies. Both O and Ti vacancies can trap the injected electron albeit at very different time scales. Finally the O vacancies could increase the charge recombination at the interface.

Because the surface terminations are not well controlled in the TiO_2-based DSSCs, different surface terminations invariably occur in a batch of DSSCs, which could lead to large variations of ET rates and the performance of the solar cells. Therefore it is of crucial importance to optimize the surface termination in order to achieve uniformity of the performance. The native surface defects (O vacancies) can significantly influence the performance of DSSCs—both positively and negatively. Thus, one has to exploit the positive aspects and concomitantly avoid the negative ones. It is in this regard that the theoretical effort reported in this paper and the similar ones could prove useful for the future development of DSSCs.

Acknowledgment. We thank Professor Oleg V. Prezhdo for valuable discussions. This work was supported by NSF Grants DMR-0611562 and DMR-0958596.

References and Notes

(1) O'regan, B.; Grätzel, M. *Nature* **1991**, *353*, 737–740.
(2) Peet, J.; Kim, J. Y.; Coates, N. E.; Ma, W. L.; Moses, D.; Heeger, A. J.; Bazan, G. C. *Nat. Mater.* **2007**, *6*, 497–500.
(3) Huber, R.; Sporlein, S.; Moser, J. E.; Grätzel, M.; Wachtveitl, J. *J. Phys. Chem. B* **2000**, *104*, 8995–9003.
(4) Hao, E. C.; Anderson, N. A.; Asbury, J. B.; Lian, T. Q. *J. Phys. Chem. B* **2002**, *106*, 10191–10198.
(5) Matylitsky, V. V.; Lenz, M. O.; Wachtveitl, J. *J. Phys. Chem. B* **2006**, *110*, 8372–8379.
(6) Di Lorio, Y.; Brusa, M. A.; Feldhoff, A.; Grela, M. A. *ChemPhysChem* **2009**, *10*, 1077–1083.
(7) Diebold, U. *Surf. Sci. Rep.* **2003**, *48*, 53–229.
(8) Shapovalov, V.; Wang, Y.; Truong, T. N. *Chem. Phys. Lett.* **2003**, *375*, 321–327.
(9) Zhang, Z.; et al. *Langmuir* **2004**, *20*, 4954–4969.
(10) Zhao, J.; Li, B.; Onda, K.; Feng, M.; Petek, H. *Chem. Rev.* **2006**, *106*, 4402–4427.
(11) Wendt, S.; Sprunger, P. T.; Lira, E.; Madsen, G. K. H.; Li, Z. S.; Hansen, J. O.; Matthiesen, J.; Blekinge-Rasmussen, A.; Laegsgaard, E.; Hammer, B.; Besenbacher, F. *Science* **2008**, *320*, 1755–1759.
(12) Di Valentin, C.; Pacchioni, G.; Selloni, A. *Phys. Rev. Lett.* **2006**, *97*, 166803.
(13) Ganduglia-Pirovano, M. V.; Hofmann, A.; Sauer, J. *Surf. Sci. Rep.* **2007**, *62*, 219–270.
(14) Cheng, H. Z.; Selloni, A. *Phys. Rev. B* **2009**, *79*, 092101.
(15) Meng, S.; Kaxiras, E. *Nano Lett.* **2010**, *10*, 1238–1247.
(16) Willig, F.; Zimmermann, C.; Ramakrishna, S.; Storck, W. *Electrochim. Acta* **2000**, *45*, 4565–4575.
(17) Asbury, J. B.; Hao, E.; Wang, Y. Q.; Ghosh, H. N.; Lian, T. Q. *J. Phys. Chem. B* **2001**, *105*, 4545–4557.
(18) Huber, R.; Moser, J. E.; Grätzel, M.; Wachtveitl, J. *J. Phys. Chem. B* **2002**, *106*, 6494–6499.
(19) Zimmermann, C.; Willig, F.; Ramakrishna, S.; Burfeindt, B.; Pettinger, B.; Eichberger, R.; Storck, W. *J. Phys. Chem. B* **2001**, *105*, 9245–9253.
(20) Benko, G.; Kallioinen, J.; Korppi-Tommola, J. E. I.; Yartsev, A. P.; Sundstrom, V. *J. Am. Chem. Soc.* **2002**, *124*, 489–493.
(21) Gundlach, L.; Ernstorfer, R.; Willig, F. *Prog. Surf. Sci.* **2007**, *82*, 355–377.
(22) Ramakrishna, S.; Willig, F.; May, V.; Knorr, A. *J. Phys. Chem. B* **2003**, *107*, 607–611.
(23) Li, J. R.; Nilsing, M.; Kondov, I.; Wang, H. B.; Persson, P.; Lunell, S.; Thoss, M. *J. Phys. Chem. C* **2008**, *112*, 12326–12333.
(24) Rego, L. G. C.; Batista, V. S. *J. Am. Chem. Soc.* **2003**, *125*, 7989–7997.

(25) Abuabara, S. G.; Rego, L. G. C.; Batista, V. S. *J. Am. Chem. Soc.* **2005**, *127*, 18234–18242.
(26) Craig, C. F.; Duncan, W. R.; Prezhdo, O. V. *Phys. Rev. Lett.* **2005**, *95*, 163001.
(27) Meng, S.; Ren, J.; Kaxiras, E. *Nano Lett.* **2008**, *8*, 3266–3272.
(28) Persson, P.; Lundqvist, M. J.; Ernstorfer, R.; Goddard, W. A.; Willig, F. *J. Chem. Theory Comput.* **2006**, *2*, 441–451.
(29) Stier, W.; Prezhdo, O. V. *Isr. J. Chem.* **2002**, *42*, 213–224.
(30) Stier, W.; Prezhdo, O. V. *J. Phys. Chem. B* **2002**, *106*, 8047–8054.
(31) Stier, W.; Prezhdo, O. V. *THEOCHEM* **2003**, *630*, 33–43.
(32) Stier, W.; Duncan, W. R.; Prezhdo, O. V. *Adv. Mater.* **2004**, *16*, 240–+.
(33) Duncan, W. R.; Stier, W. M.; Prezhdo, O. V. *J. Am. Chem. Soc.* **2005**, *127*, 7941–7951.
(34) Duncan, W. R.; Craig, C. F.; Prezhdo, O. V. *J. Am. Chem. Soc.* **2007**, *129*, 8528–8543.
(35) Duncan, W. R.; Prezhdo, O. V. *J. Am. Chem. Soc.* **2008**, *130*, 9756–9762.
(36) Prezhdo, O. V.; Duncant, W. R.; Prezhdo, V. V. *Acc. Chem. Res.* **2008**, *41*, 339–348.
(37) Prezhdo, O. V.; Duncan, W. R.; Prezhdo, V. V. *Prog. Surf. Sci.* **2009**, *84*, 30–68.
(38) Ramakrishna, S.; Willig, F. *J. Phys. Chem. B* **2000**, *104*, 68–77.
(39) Thoss, M.; Kondov, I.; Wang, H. B. *Chem. Phys.* **2004**, *304*, 169–181.
(40) Wang, L. X.; May, V. *J. Chem. Phys.* **2004**, *121*, 8039–8049.
(41) De Angelis, F.; Fantacci, S.; Selloni, A.; Nazeeruddin, M. K.; Gratzel, M. *J. Am. Chem. Soc.* **2007**, *129*, 14156–14157.
(42) De Angelis, F.; Fantacci, S.; Selloni, A.; Gratzel, M.; Nazeeruddin, M. K. *Nano Lett.* **2007**, *7*, 3189–3195.
(43) Doltsinis, N. L.; Marx, D. *J. Theor. Comput. Chem.* **2002**, *1*, 319–349.
(44) Tully, J. C. *J. Chem. Phys.* **1990**, *93*, 1061–1071.
(45) Drukker, K. *J. Comput. Phys.* **1999**, *153*, 225–272.
(46) Parandekar, P. V.; Tully, J. C. *J. Chem. Phys.* **2005**, *122*, 094102.
(47) Schmidt, J. R.; Parandekar, P. V.; Tully, J. C. *J. Chem. Phys.* **2008**, *129*, 044104.
(48) Redfern, P. C.; Zapol, P.; Curtiss, L. A.; Rajh, T.; Thurnauer, M. C. *J. Phys. Chem. B* **2003**, *107*, 11419–11427.
(49) Kresse, G.; Hafner, J. *Phys. Rev. B* **1993**, *47*, 558–561.
(50) Kresse, G.; Furthmuller, J. *Phys. Rev. B* **1996**, *54*, 11169–11186.
(51) Perdew, J. P.; Burke, K.; Wang, Y. *Phys. Rev. B* **1996**, *54*, 16533–16539.
(52) Duncan, W. R.; Prezhdo, O. V. *J. Phys. Chem. B* **2005**, *109*, 365–373.
(53) Cho, E.; Han, S.; Ahn, H.-S.; Lee, K.-R.; Kim, S. K.; Hwang, C. S. *Phys. Rev. B* **2006**, *73*, 193202.
(54) Janotti, A.; Varley, J. B.; Rinke, P.; Umezawa, N.; Kresse, G.; Van de Walle, C. G. *Phys. Rev. B* **2010**, *81*, 085212.
(55) Kruger, P.; Bourgeois, S.; Domenichini, B.; Magnan, H.; Chandesris, D.; Le, Fevre, P.; Flank, A. M.; Jupille, J.; Floreano, L.; Cossaro, A.; Verdini, A.; Morgante, A. *Phys. Rev. Lett.* **2008**, *100*, 055501.

JP108590F